The effect of strong nonlinearity on wave-induced vertical mixing

Maciej Paprota[1,*] and Wojciech Sulisz[1,*]

[1]Department of Wave Mechanics and Structural Dynamics, Institute of Hydro-Engineering, Polish Academy of Sciences, ul. Kościerska 7, 80-328, Gdańsk, Poland
[*]These authors contributed equally to this work.

Correspondence: Maciej Paprota (mapap@ibwpan.gda.pl)

Abstract. A semi-analytical solution to advection-diffusion equation is coupled with a ~~pseudo-spectral approach to~~ nonlinear wavemaker model to investigate the effect of strong nonlinearity on wave-induced mixing. The comparisons with weakly-nonlinear model predictions reveal that in the case of waves of higher steepness, enhanced mixing affects subsurface layer of the water column. Including higher-order terms into free-surface boundary conditions of the wavemaker problem secures reliable estimation of the time-mean velocity field. The corrected wave-induced mass-transport velocity leads to improved estimates of subsurface mixing intensity and ocean surface temperature.

1 Introduction

Mass-transport processes associated with the propagation of non-breaking ocean surface waves strongly affect the mixing of oceanic waters and the global exchange of heat at the air-water interface. Surface waves transfer energy into turbulence modifying the mixing intensity of the upper ocean (Qiao et al., 2004, 2010, 2013). Therefore, the correct identification and quantification of mass-transport processes associated with water waves leading to mixing of subsurface ocean waters is of practical importance for short-term and long-term weather forecasts.

Small-scale and large-scale climate modelling equally benefits from including the wave-induced mixing predictions into the general ocean circulation simulations (e.g. Qiao et al., 2004; Xia et al., 2006). Including the parameterized wave-induced mixing in ocean circulation models confirms that its contribution qualitatively improves the reliability of numerical results (e.g. Song et al., 2007; Shu et al., 2011). Despite the fact that some field measurements lead to the conclusion that surface waves contribute to heat exchange of the upper ocean (Matsuno et al., 2006), it is difficult to collect reliable *in situ* data confirming the role of non-breaking surface waves in vertical mixing processes. An alternative approach to the problem is to investigate the wave-induced mixing based on the physical tests in the wave flume or the wave basin.

Laboratory experiments are the source of valuable information on wave induced-mixing processes as well as they provide data supporting the evaluation of wave-induced mixing coefficient (e.g. Babanin and Haus, 2009; Dai et al., 2010; Sulisz and Paprota, 2015). In the wave flume, the mixing originated from breaking and non-breaking wave processes may be eventually separated to evaluate the real contribution from the non-breaking surface waves to general ocean circulation, which is of fundamental importance for calibration of wave-induced mixing models (Sulisz and Paprota, 2019). It should be noted that the

experimental data are affected by undesirable spurious laboratory effects requiring special attention when analyzing the results of mass-transport processes driven by waves (e.g. Paprota and Sulisz, 2018; Paprota, 2020).

The ~~present study~~ study presents the methods of the analysis of wave-induced vertical mixing from the wavemaker perspective. The derived mathematical modelling approach may be directly applied to experimental research aiming at recognising, quantifying, and parameterising wave-induced vertical mixing effects (see e.g. Dai et al., 2010; Sulisz and Paprota, 2015) for a better design of physical model setup and the selection of wave parameters selection in the laboratory. The awareness of the influence of laboratory side effects on the experimental outcome is essential for correct interpretation of achieved results. This issue was raised in the earlier studies (Sulisz and Paprota, 2015, 2019).

The study extends the analysis of wave-induced vertical mixing performed by Sulisz and Paprota (2019) on the basis of weakly-nonlinear theory applied to mechanically generated water waves. The improvements cover the application of the more exact nonlinear wavemaker model, which was successfully verified with respect to kinematics of regular waves against laboratory measurements collected in the flume (Paprota and Sulisz, 2018; Paprota, 2020). This higher-order method allows modelling of non-breaking waves with strong nonlinearities and admits amplitude dispersion, nonlinear wave-wave interactions in deep and intermediate waters as well as solitary waves propagation, which goes far beyond the applicability of weakly-nonlinear approaches. Corresponding methods basing on a pseudo-spectral approach, which consider highly-nonlinear non-breaking waves (Dommermuth and Yue, 1987; West et al., 1987) – (see also Paprota and Sulisz, 2019, for a review).

This should lead to more accurate estimation of the phase-averaged wave velocity field and, hopefully, the more reliable evaluation of the evolving water temperature field under regular waves. In this way, it is possible to separate the Stokes drift from Lagrangian and Eulerian mean velocities (see Paprota et al., 2016; Paprota and Sulisz, 2018; Paprota, 2020). Hence, the results presented in this study may improve simple models of Stokes drift parametrization for random ocean waves (Myrhaug et al., 2018), while the derived modelling framework may be modified to cover open ocean conditions in a large periodic domain (Paprota, 2019).

New contributions are also presented with regard to the methods of calculations of time-mean flows, which are essential for the present analyses. Namely, a new Eulerian procedure is reported, which is different to Lagrangian-based method applied in earlier studies (Paprota et al., 2016; Paprota and Sulisz, 2018; Paprota, 2020). The study also highlights the differences between two methods of calculation of velocity distribution of time-mean wave-induced flows either based on Lagrangian particle tracking or approximated Eulerian averaging. In case of the former, an improved and more accurate procedure of estimating the phase-averaged velocity is developed.

The paper is composed as follows. First, the outline of the coupled theoretical model describing the mixing processes under mechanically induced water waves is presented. Then, the comprehensive comparison between weakly and fully nonlinear approaches is given using numerical results to evaluate the effects of strong nonlinearity on vertical mixing processes. Finally, the discussion on the major results is provided together with remarks on accuracy and reliability of mathematical and numerical methods together with further discussions on putting the results of the study in a broader context of earth system modeling with respect to general ocean circulation. The paper is then completed by a summary and conclusions.

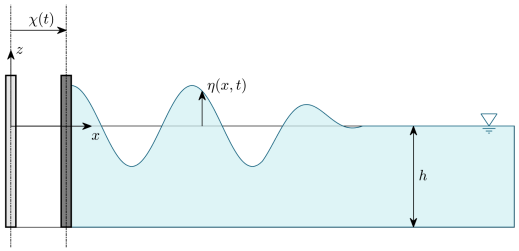

Figure 1. Schematic view of ~~meachanically-generated~~ mechanically-generated waves and the coordinate system.

2 Materials and Methods

The considered numerical approach to the modeling of vertical mixing induced by mechanically generated waves is realized through a procedure involving two fundamental steps referring to the solution of the wavemaker problem and advection-diffusion balance, respectively.

2.1 Particle kinematics of mechanically-generated waves

First, the problem of the generation of waves in a ~~laboratory~~ numerical wave flume is formulated and solved. In the present study, a potential flow wave theory is used to obtain the solution within the Eulerian frame of reference. Weakly-nonlinear analytical approach and higher-order numerical methods are employed to determine the wave fields in the rectangular domain, in which the water elements are defined by the horizontal x and vertical z coordinates of the Cartesian system. The origin of the system is located at the intersection of the wavemaker zero position and free-surface level corresponding to the hydrostatic conditions. The mechanically-driven oscillation of the free surface represented by elevation function $\eta(x,t)$ is induced by the piston-like motion of the wavemaker paddle according to the displacement function $\chi(t)$. The flume bottom is assumed horizontal and the water depth is $h = const$. The general presentation of the computational domain and the location of the coordinate system is depicted in Fig. 1.

According to the potential flow assumptions, the motion of the inviscid and incompressible fluid is irrotational. Moreover, the solid boundaries are impervious. The scalar velocity potential function $\phi(x,z,t)$ may be introduced to determine the velocity vector field $\mathbf{v}(x,z,t)$ such that $\mathbf{v} = \nabla\phi$. The wavemaker boundary-value problem is then formulated as

$$\nabla^2\phi = 0, \qquad -h \le z \le \eta, \tag{1}$$

$$\eta_t + \phi_x\eta_x - \phi_z = 0, \qquad z = \eta, \tag{2}$$

$$\phi_t + \frac{1}{2}(\phi_x^2 + \phi_z^2) + g\eta = 0, \qquad z = \eta, \tag{3}$$

$$\phi_z = 0, \qquad z = -h, \tag{4}$$

$$\chi_t - \phi_x = 0, \qquad x = \chi, \tag{5}$$

where g is the acceleration due to gravity.

The first part of a solution procedure involves expanding the kinematic free-surface boundary condition (2), the dynamic free-surface boundary condition (3), and the kinematic wavemaker boundary condition (5) in a Taylor series about a mean position corresponding to the still water level ($z = 0$) for (2)-(3) and wavemaker paddle zero position ($x = 0$) for (5)

$$\sum_{m=0} \frac{\eta^m}{m!} \frac{\partial^m}{\partial z^m}(\eta_t + \phi_x \eta_x - \phi_z) = 0, \qquad z = 0, \tag{6}$$

$$\sum_{m=0} \frac{\eta^m}{m!} \frac{\partial^m}{\partial z^m}(\phi_t + \frac{1}{2}(\phi_x^2 + \phi_z^2) + g\eta) = 0, \qquad z = 0, \tag{7}$$

$$\sum_{m=0} \frac{\chi^m}{m!} \frac{\partial^m}{\partial z^m}(\chi_t - \phi_x) = 0, \qquad x = 0. \tag{8}$$

In this way, a simple rectangular form of the computational domain is preserved and the solution procedure is advanced further using either the perturbation or spectral approach. In the present study both weakly-nonlinear (perturbation expansions) and higher-order (spectral expansions) solutions are briefly presented and applied to calculate the velocity field for wave-induced mixing calculations.

2.1.1 Weakly-nonlinear solution

The perturbation expansion is first applied to solve the wavemaker problem defined by Eqs. (1)-(5) according to the solution derived by Hudspeth and Sulisz (1991); Sulisz and Hudspeth (1993). The monochromatic wavemaker paddle displacement of amplitude s is assumed

$$\chi(t) = s\sin(\sigma t + \varphi), \tag{9}$$

which generates periodic waves of the first-order amplitude of a, the angular frequency of σ, and the phase φ in the semi-infinite flume domain. Due to the fact that x goes to infinity, the radiation condition is imposed at the far end lateral boundary of the domain (Hudspeth and Sulisz, 1991).

Using the expansions of the boundary conditions Eqs. (6)-(8) and retaining the terms up to the second order, the weakly-nonlinear boundary conditions become

$$\eta_t - \phi_z + \phi_x \eta_x - \eta \phi_{zz} = 0, \qquad z = 0, \tag{10}$$

$$\phi_t + \frac{1}{2}(\phi_x^2 + \phi_z^2) + \eta \phi_{zt} + g\eta = 0, \qquad z = 0, \tag{11}$$

$$\chi_t - \phi_x - \chi \phi_{xx} = 0, \qquad x = 0. \tag{12}$$

Additionally, the following small steepness parameter $\epsilon = ak$ (where k is the first-harmonic wave number) perturbation expansions of the angular frequency ω ($\sigma = \omega_0$), the free-surface elevation, and the velocity potential functions are used (Hudspeth and Sulisz, 1991)

$$\omega = \sum_{n=0} \epsilon^n \omega_n, \tag{13}$$

$$\phi(x, z, t) = \sum_{n=0} \epsilon^n {}_{n+1}\phi(x_{n+1}, z, t), \tag{14}$$

$$\eta(x, t) = \sum_{n=0} \epsilon^n {}_{n+1}\eta(x, t)_{n+1}. \tag{15}$$

Substituting the perturbation forms Eqs. (13)-(15) into the boundary conditions correct up to the second order, Eqs. (10)-(12), leads to the final weakly-nonlinear solution to the velocity potential and free-surface elevation functions (Hudspeth and Sulisz, 1991). The formulas for the horizontal $U(x, y)$ and vertical $V(x, y)$ components of the time-independent mass-transport velocity $\mathbf{V}(x, y)$ for the case of the piston-type wavemaker of full-depth draught are calculated from nondimensional forms reported as in Eqs. (50a) and (50b) by Hudspeth and Sulisz (1991). In order to get dimensional values, the results calculated by Eqs. (50a) and (50b) in the work by Hudspeth and Sulisz (1991) are multiplied by $a\sqrt{gk}$.

Far away from the wavemaker paddle ($x > 3h$), the vertical component of the time-independent velocity vanishes and the time-independent horizontal velocity profile along the water depth U_L converges to the sum of the Stokes drift U_S and return current U_E velocities (Longuet-Higgins, 1953; Dean and Dalrymple, 1984), i.e.

$$U_L(z) = U_S(z) + U_E, \tag{16}$$

where the Stokes drift profile is calculated as

$$U_S(z) = \frac{k\sigma a^2 \cosh(2k(z+h))}{2\sinh^2(kh)}, \tag{17}$$

and the return current value takes the form

$$U_E = -\frac{k\sigma a^2 \sinh(2kh)}{4kh \sinh^2(kh)} = -\frac{a^2 kg}{2\sigma h}. \tag{18}$$

2.1.2 Higher-order nonlinear solution

An alternative approach, which admits higher-order wave components, is based on the spectral method applied to the wavemaker problem (Paprota and Sulisz, 2018). Contrary to the presented perturbation approach, the waves are generated by an arbitrary function $\chi(t)$ in a finite domain of length b which is taken sufficiently large to exclude the effect of wave reflection from the far end wall of the flume. In this regard, only progressive waves are considered facilitating the comparisons with the weakly-nonlinear solution.

The free-surface elevation function is expanded in a Fourier cosine series as

$$\eta(x,t) = \sum_{i=0} a_i \cos(\lambda_i x), \tag{19}$$

while the corresponding expansion of the velocity potential function is coupled with an additional term satisfying the wavemaker boundary condition (5) to give

$$\begin{aligned}\phi(x,z,t) = &\sum_{i=0} A_i \frac{\cosh(\lambda_i(z+h))}{\cosh(\lambda_i h)} \cos(\lambda_i x) + B_0((x-b)^2 - (z+h)^2) \\ &+ \sum_{j=1} B_j \frac{\cosh(\mu_j(x-b))}{\cosh(\mu_j b)} \cos(\mu_j(z+h)),\end{aligned} \tag{20}$$

where $\lambda_i = i\pi/b$ and $\mu_j = j\pi/h$ are the eigenvalues of the expansions and the solution coefficients are the functions of time ($a_i(t)$, $A_i(t)$, and $B_j(t)$). The B_j coefficients are determined as (Paprota and Sulisz, 2018)

$$B_0 = \frac{\chi_t h + \sum_{m=1}^{M} \frac{\chi^m}{m!} \sin\frac{m\pi}{2} \sum_{i=0} \lambda_i^m A_i \tanh(\lambda_i h)}{2h(\chi - b)}, \tag{21}$$

$$B_j = \frac{-2\cos(\mu_j h) \sum_{m=1}^{M} \frac{\chi^m}{m!} \sin(\frac{m\pi}{2}) \sum_{i=0} \frac{\lambda_i^{m+2}}{\lambda_i^2+\mu_j^2} A_i \tanh(\lambda_i h)}{h \sum_{m=0}^{M} \mu_j^{m+1} \frac{\chi^m}{m!} \cos(m\pi) \tanh(\mu_j b)^{|\cos\frac{m\pi}{2}|}}, \qquad j > 0. \tag{22}$$

The coefficients A_i, B_j, and a_i are determined in an iterative solution procedure from the kinematic free-surface boundary condition (6), the dynamic free-surface boundary condition (7), and the kinematic wavemaker boundary condition (8). For a given time t, the uknown coefficients a_i, A_i ~~, and B_j~~ are calculated using Fourier transform of η and ϕ ~~together with~~ as

$$a_i = \frac{2}{b} \int_0^b \eta(x,t) \cos(\lambda_i x)\, \mathrm{d}x, \quad A_i = \frac{2}{b} \int_0^b \phi(x,0,t) \cos(\lambda_i x)\, \mathrm{d}x, \tag{23}$$

while B_j are determined using Eqs. (21) and (22). Time-stepping is then applied to obtain values of ϕ and η at a new time level. A fourth-order Adams-Bashforth-Moulton predictor-corrector approach is prefered as a time-marching scheme (see e.g. Press et al., 1988), with initial values of $\phi(x,0,0) = 0$ and $\eta(x,0) = 0$. The wavemaker model used in the present study is reported in the work of Paprota and Sulisz (2018).

The instantaneous wave velocity field is derived by expressing the horizontal u and vertical w velocity components in terms of the spatial derivatives of the velocity potential ϕ_x and ϕ_z respectively as

$$u(x,z,t) = -\sum_{i=0} \lambda_i A_i \frac{\cosh(\lambda_i(z+h))}{\cosh(\lambda_i h)} \sin(\lambda_i x) + 2B_0(x-b) + \sum_{j=1} \mu_j B_j \frac{\sinh(\mu_j(x-b))}{\cosh(\mu_j b)} \cos(\mu_j(z+h)), \tag{24}$$

$$w(x,z,t) = \sum_{i=0} \lambda_i A_i \frac{\sinh(\lambda_i(z+h))}{\cosh(\lambda_i h)} \cos(\lambda_i x) - 2B_0(z+h) - \sum_{j=1} \mu_j B_j \frac{\cosh(\mu_j(x-b))}{\cosh(\mu_j b)} \sin(\mu_j(z+h)). \tag{25}$$

After the steady state of fully-developed wave motion is achieved, the time-independent wave velocity field may be approximated by time-averaging of the instantaneous wave velocity within the range limited by two in-phase states of regular wave motion (over one wave period) as

$$U(x,z) = \left\langle u_x \int u dt + u_z \int w dt + 0.5u_{xx}\left(\int u dt\right)^2 + 0.5u_{zz}\left(\int w dt\right)^2 \right\rangle + \langle u \rangle, \tag{26}$$

$$W(x,z) = \left\langle w_x \int u dt + w_z \int w dt + 0.5w_{xx}\left(\int u dt\right)^2 + 0.5w_{zz}\left(\int w dt\right)^2 \right\rangle + \langle w \rangle. \tag{27}$$

and is referred here and after as the Eulerian-mean transport velocity (EMTV). The pair of triangle brackets $<>$ denotes the operator of time-averaging over one wave period. The velocities u and w are calculated using Eqs. (23) and (24), while their derivatives are evaluated analytically. The integrals of u and w are determined directly from Eqs. (23) and (24) upon replacing the time-dependent coefficients A_i and B_j with their integrals $\int A_i dt$ and $\int B_j dt$. The integration is achieved by expanding the A_i and B_j into a Fourier series with respect to time and integrating the resulting Fourier expansions analytically.

An alternative approach, which leads to the time-independent wave velocity field, is the procedure involving the Lagrangian particle tracking - Lagrangian-mean transport velocity (LMTV). The time-averaged velocity is calculated based on the displacement of water particle moving between its two successive in-phase positions along the particle trajectory (Paprota et al., 2016). The trajectory of a water particle is determined by numerical integration of the system of differential equations

$$\frac{\mathrm{d}x}{\mathrm{d}t} = u(x,z,t), \tag{28}$$

$$\frac{\mathrm{d}z}{\mathrm{d}t} = w(x,z,t), \tag{29}$$

for the set of initial particle locations.

In the present study, the improvements to the method of evaluation of mass transport velocity based on the Lagrangian particle tracking (Paprota and Sulisz, 2018) are introduced. In ~~order to get better estimation of the time-independent velocity field, the two hydrodynamic states corresponding to both zero up- and down-crossings of the regular wave are used to start-up the tracking procedure - contrary to the previous method based only on the zero down-crossing initial position (e.g. Paprota et al., 2016; Paprota and Sulisz, 2018)~~the previous works (Paprota et al., 2016; Paprota and Sulisz, 2018; Paprota, 2020), the procedure relied on distributing artificial tracers in a water column under fully developed regular waves. Initially, the tracers are uniformly distributed along the water depth and they coincide with ~~either the zero up-crossing or zero~~ the zero down-crossing phase of the wave for a given distance from the wavemaker. ~~Then, the~~ After one Lagrangian wave period (see e.g. Longuet-Higgins, 1986; Chen et al., 2009), the tracers move from their original position due to mass transport. The particle tracking procedure is employed to determine the mass transport velocity profile. The procedure is repeated for subsequent longitudinal positions to cover the accepted region of interest. ~~Finally, the~~

Here, in order to get the better estimation of the time-independent velocity field, the two hydrodynamic states corresponding to both zero up- and down-crossings of the regular wave are used to start-up the tracking procedure - contrary to the previous method based only on the zero down-crossings (e.g. Paprota et al., 2016; Paprota and Sulisz, 2018). The procedure is analogous, but involves more tracers and covers two phase positions. The resulting LMTV is calculated as the mean of the time-independent velocity fields corresponding to both zero-crossing initial states.

2.2 Wave-induced vertical mixing intensity

The numerical solution to the two-dimensional advection-diffusion equation with relevant boundary conditions is used to predict evolution of temperature field under mechanically generated regular waves in a flume. Assuming that the changes of temperature are solely due to wave-induced and diffusion processes, the following boundary-value problem is formulated as in the work by Sulisz and Paprota (2019)

$$T_t + UT_x + WT_z = \partial_x(\kappa T_x) + \partial_z(\kappa T_z), \tag{30}$$

$$T_z = 0, \qquad z = 0, \tag{31}$$

$$T_x = 0, \qquad x = 0, \tag{32}$$

$$T_z = 0, \qquad z = -h, \tag{33}$$

$$T_x = 0, \qquad x = b, \tag{34}$$

where T is the water temperature, and κ is the diffusion coefficient represented as a sum of the molecular (κ_m) and wave-induced (κ_v) diffusivities

$$\kappa = \kappa_m + \kappa_v. \tag{35}$$

In advection-diffusion equation (29) the velocities U and W are, in fact, Lagrangian velocities which describe mean transport velocity field (Stokes drift and the return current in this case). The inclusion of Stokes drift (without return current) to advection equation was discussed explicitly for the case of ocean waves by McWilliams and Sullivan (2000).

The molecular diffusivity $\kappa_m = 1.4 \times 10^{-7}\text{m/s}^2$, while the wave-induced diffusivity is calculated by the formula reported by Sulisz and Paprota (2015) as

$$\kappa_v(z) = \alpha a^3 k\sigma \frac{\sinh^2(k(z+h))\cosh(k(z+h))}{\sinh^3(kh)}, \tag{36}$$

where ~~α~~ $\alpha = 0.002$ is the dimensionless coefficient, which is evaluated based on measurements ~~.~~ (Sulisz and Paprota, 2015). The derivation of κ_v is based on the weakly-nonlinear theory. More information is provided in the work of Sulisz and Paprota (2015) , where the comparison between weakly-nonlinear and more general form is provided. The parameter α was estimated based on the experiments only for the presented form of κ_v. In order to use a more general formula, new values of α must be determined using experimental data from a wider range of wave conditions.

The advection-diffusion equation Eq.(29) holds in the entire fluid domain, while the heat radiation is assumed zero at the water surface - Eq.(30), the bottom - Eq.(32), and the lateral boundaries - Eqs.(31) and (33). The length b is taken sufficiently long in order to reduce the effect of the finite domain on the results in the area of interest, which is limited to the region of several water depths from the wavemaker paddle. The omitted procedure of incorporating the non-zero heat radiation at the water surface is discussed in the paper by Sulisz and Paprota (2019).

The solution of the advection-diffusion equation Eq.(29) is achieved by employing a similar methodology which is used to solve the wavemaker problem admitting higher-order nonlinearities presented in the previous section. Accordingly, the scalar temperature field function is expanded into a double Fourier series of the form (Sulisz and Paprota, 2019)

$$T(x,z,t) = \sum_{i=1}\sum_{j=1} d_{ij}\cos(\lambda_i(x-b))\cos(\mu_j(z+h)). \tag{37}$$

Again, the solution of Eq. (29) is achieved by a time-stepping procedure, which, in this case, consists of an application of the spectral expansion method to describe T and the Runge-Kutta formulas to proceed in time (see e.g. Press et al., 1988). Accordingly, the wave-induced diffusivity is determined using Eq. (35), while the velocity field is either calculated by means of the weakly-nonlinear solution (Hudspeth and Sulisz, 1991) or higher-order approach (Paprota and Sulisz, 2018) for selected wave parameters. The initial condition of given vertical temperature distribution $T_0(z)$ is used to start-up the time stepping procedure. The time derivative of temperature T is calculated from Eq. (29) with the aid of the expansion Eq. (36) after the coefficients d_{ij} are determined by applying a two-dimensional cosine fast Fourier transform.

Table 1. Basic dimensionless parameters of mechanically-generated regular waves.

Depth parameter kh	Height-depth ratio H/h	Steepness parameter Ak	Wave-iinduced diffusivity $\kappa_v(0)/\kappa_m$	Ursell number HL^2/h^3
0.5	0.05	0.0125	0.36	7.9
0.5	0.1	0.025	2.91	15.8
0.5	0.2	0.05	23.3	31.6
1	0.05	0.025	0.8	1.97
1	0.1	~~0.5~~ 0.05	6.4	3.95
1	0.2	0.1	51.3	7.9
2	0.05	0.05	2.01	0.49
2	0.1	0.1	16.1	0.99
2	0.2	0.2	128.9	1.97

3 Results and discussion

The evaluation of temperature evolution of an oscillating water body is analyzed in a numerical wave flume environment. This approach provides a basis for the straightforward verification of the major outcome against measurements in the real laboratory. On the other hand, the numerical model may be modified to cover pseudo-random ocean waves in a large periodic domain (see e.g. Paprota, 2019) to analyze the wave-induced vertical mixing processes in offshore conditions.

3.1 Numerical test cases

The waves are generated by a monochromatic wavemaker motion in a numerical flume. The transitional and shallow water wave cases are considered for three depth-relative dimensionless parameters kh of 0.5, 1 and 2. The effect of wave height H is also studied and corresponds to the dimensionless steepness parameter H/h of 0.05, 0.1 and 0.2. In the case of the higher-order solution, the waves are generated starting from rest with the ramp function applied to the stroke of the wavemaker motion for the first five wave periods. As previously stated, the longitudinal size of the flume b is taken sufficiently long to exclude wave reflections from the analysis and it corresponds to ten wavelengths (L) for $kh = 2$ and $20L$ in the remaining longer wave cases. The selected progressive wave parameters are in accordance to previous studies on the modeling of wave-induced mixing in wave flumes (Sulisz and Paprota, 2019). After the steady state is achieved, the time-independent wave velocity field is determined. The resulting horizontal and vertical velocity components U and W are then substituted to Eq. (29) and the temperature field evolution is predicted. The summary of wave parameters is provided in Table 1 together with wave-induced diffusivity values at the surface in relation to molecular diffusivity.

It should be noted that the model may be applied to deep-water as well as shallow water conditions, which was already presented in the work by Sulisz and Paprota (2015). Here, we analyse transitional waves of kh from 0.5 to 2.0. In this

way, the results from our previous work (Sulisz and Paprota, 2019) may be directly compared. In case of deep water waves corresponding to $kh > \pi$, the mixing would completely swept away the warmer water from the domain for the considered time frame and this case was omitted in the present study.

3.2 Phase-averaged velocity distribution

The accurate assessment of the time-independent velocity field is of significant importance in the modeling of temperature changes under undulating water surface. The increasing steepness of generated waves intensifies wave-induced mixing processes, but also changes the structure of heat fluxes distribution in the region occupied by the fluid. The analysis of phase-averaged velocity distribution in direct vicinity of the wavemaker paddle helps to identify the effect of advection terms of the Eq.(29) on the temperature evolution driven by waves.

In Figs. 2-4, time-independent velocity fields calculated by weakly-nonlinear and higher-order methods are presented. ~~In the case of the~~ The arrows represent the vectors of a phase-averaged velocity corresponding to mass-transport induced by waves. Black arrows correspond to weakly-nonlinear solution, while green and blue arrows correspond to higher-order ~~approach,~~ solution and two methods of averaging ~~of the instantaneous wave velocity field are compared graphically~~ – EMTV and LMTV, respectively (Figs. 2-4). The way of the presentation of the results is in line with the expected velocity vector field pattern, which forms half of the circulation cell limited by the air-water interface ($z/h = 0$), the wavemaker paddle ($x/h = 0$) and the bottom ($z/h = -1$). The water mass flows with the direction of wave propagation near the surface, while the adverse flow pushes the water to the wavemaker paddle in the lower part of the water column. At the wavemaker paddle, the water flows vertically forming the lateral boundary of the general circulation in the flume. Far away from the paddle, the vertical velocity components vanish and the typical mass-transport velocity profile over depth emerges as a sum of the Stokes drift Eq. (17) and the return current velocity Eq. (18). Thus, the figures are complemented by the weakly-nonlinear horizontal mass-transport velocity profile $U_L(z)$ calculated outside the direct vicinity of the wavemaker paddle Eq. (16), where the evanescent mode effect may be neglected ($x > 3h$). $U_L(z)$ is plotted at the right outer edge of the graph at $x = 3h$ for convenience of comparison.

The results presented in Fig. 2 provide information on the time-independent velocity field predicted in the direct vicinity of the wavemaker paddle and the differences between the weakly-nonlinear approach and the solution admitting higher-order terms in the most extreme nonlinear regime of shallow water ($kh = 0.5$). Due to the fact that the considered wave cases are characterized by highest values of the Ursell number, the differences between the two wavemaker models immediately appear even for the lowest amplitude of free-surface oscillations of $H/h = 0.05$ (Fig. 2a). The highest differences in the range between 10% and 20% correspond to the velocities near the wavemaker paddle and the surface, respectively. With increasing the magnitude of the surface oscillations to $H/h = 0.1$ and $H/h = 0.2$ (Figs. 2b and 2c), the differences are becoming higher in the larger area of the wavemaker paddle vicinity. The higher-order model predicts more intensive mass-transport near the bottom and the surface. The increase in the subsurface velocity and the magnitude of the current near the bottom may reach even from 15% to 30% for $H/h = 0.1$ and from 20% to 40 % for $H/h = 0.2$.

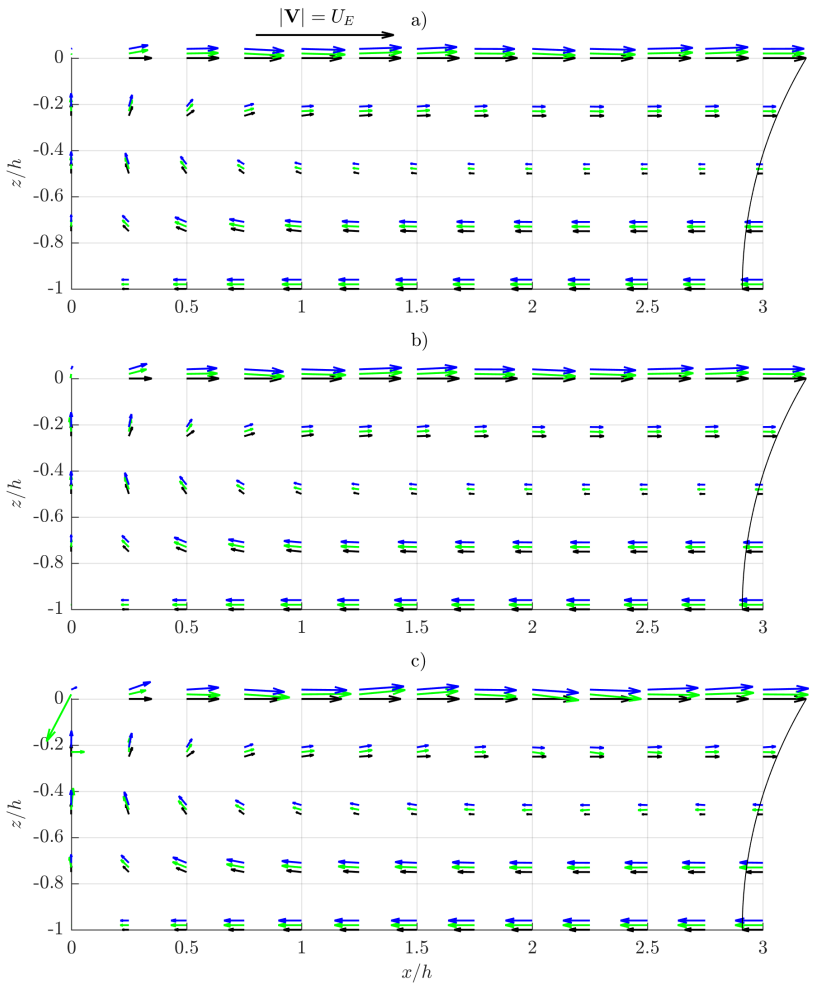

Figure 2. Time-independent velocity field under mechanically-generated regular waves characterized by $kh = 0.5$, a) $H/h = 0.05$, b) $H/h = 0.1$, c) $H/h = 0.2$; weakly-nonlinear theory - black arrows and line, higher-order theory EMTV - green arrows, LMTV - blue arrows; higher-order vectors are shifted upwards for convenience of comparison.

.

300 Some important information may be also acquired from the comparison between two methods of averaging corresponding to either Lagrangian particle tracking (LMTV) or Eulerian averaging (EMTV) basing on Eqs. 25 and 26, respectively. Although both methods of averaging provide consistent results for lower wave heights of the generated waves, EMTV results are less reliable in the case of highest waves $H/h = 0.2$ (Fig. 2c). It can be seen that the velocity vectors near the corner point determined by the intersection of the wavemaker paddle mean position and the surface ($x/h = 0$, $z/h = 0$) are unnaturally

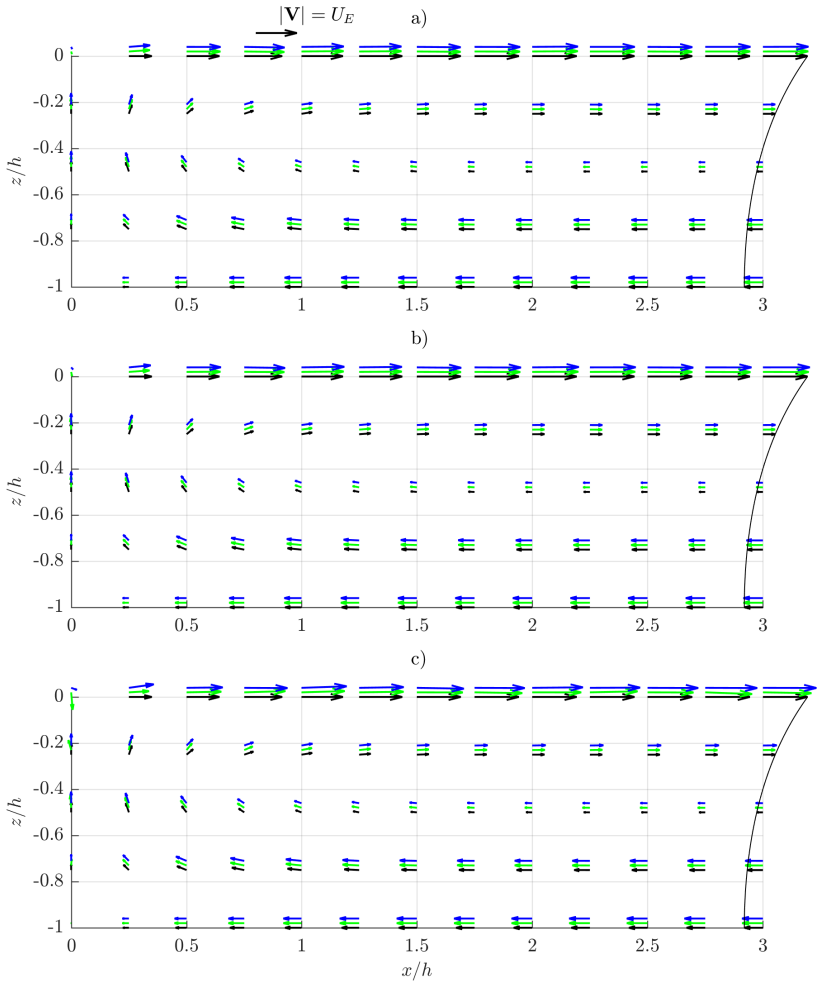

Figure 3. Time-independent velocity field under mechanically-generated regular waves characterized by $kh = 1$, a) $H/h = 0.05$, b) $H/h = 0.1$, c) $H/h = 0.2$; weakly-nonlinear theory - black arrows and line, higher-order theory EMTV - green arrows, LMTV - blue arrows; higher-order vectors are shifted upwards for convenience of comparison.

large as the velocity in this area is expected to vanish. The problems still persists when considering the subsurface velocity in some distance away from the wavemaker. The differences between the LMTV and EMTV may reach even 20% in the velocity magnitude near the intersection between the wavemaker and the surface, while even greater discrepancy is visible at corner points for the longer wave cases (Fig. 2c).

With the increasing the relative water depth (Figs. 3 and 4), the differences between weakly-nonlinear and higher-order time-independent velocity are less pronounced but still significant for steeper waves. In the case characterized by $kh = 1$, the

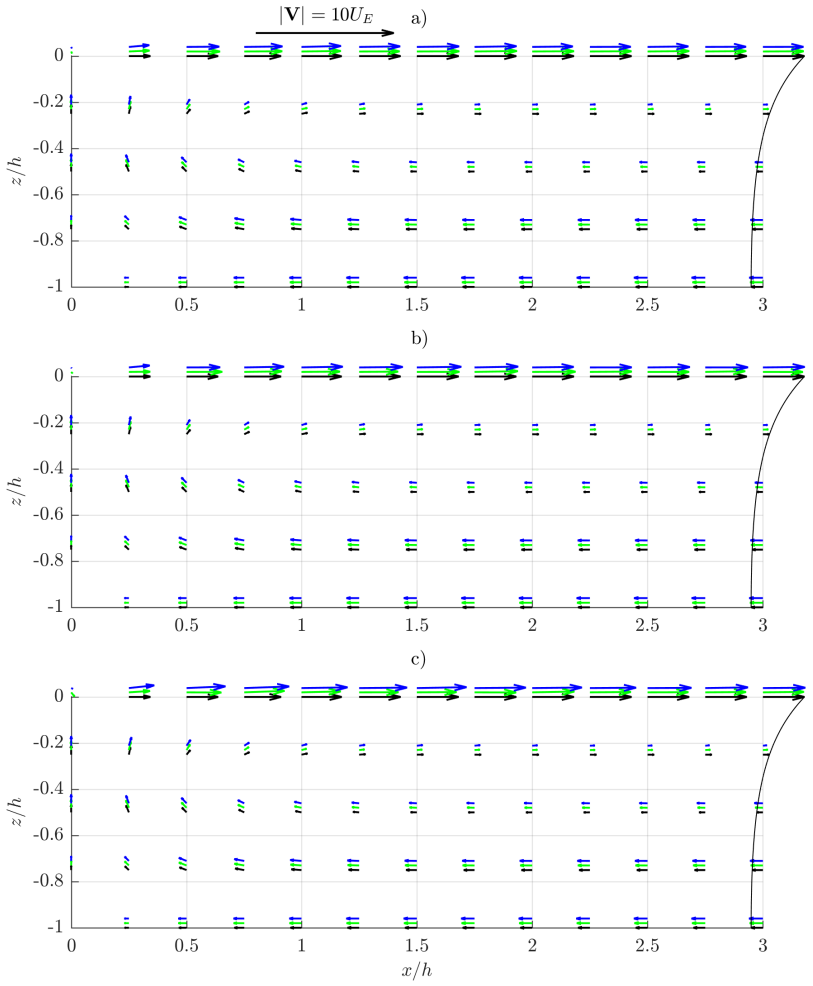

Figure 4. Time-independent velocity field under mechanically-generated regular waves characterized by $kh = 2$, a) $H/h = 0.05$, b) $H/h = 0.1$, c) $H/h = 0.2$; weakly-nonlinear theory - black arrows and line, higher-order theory EMTV - green arrows, LMTV - blue arrows; higher-order vectors are shifted upwards for convenience of comparison.

discrepancies are generally less then 10% for $H/h = 0.05$ and 0.1 ranging from 10% to 20% for the highest waves (Fig. 3ab). Again the more intensive mass circulation is apparent when higher-order terms are taken into account for the case of $kh = 1$ and $H/h = 0.2$ (Fig. 3c). The similar conclusions may be drawn for the deeper water $kh = 2$ (Fig. 4). However, in the case of the mass transport velocity profile relatively far away from the wavemaker paddle ($x = 3h$) the differences are twice as high than in the wave cases corresponding to $kh = 1$. It should be noted that, for higher kh, the results corresponding to two methods of averaging are more consistent, however the highest difference may still reach 20% as in the case of longer waves.

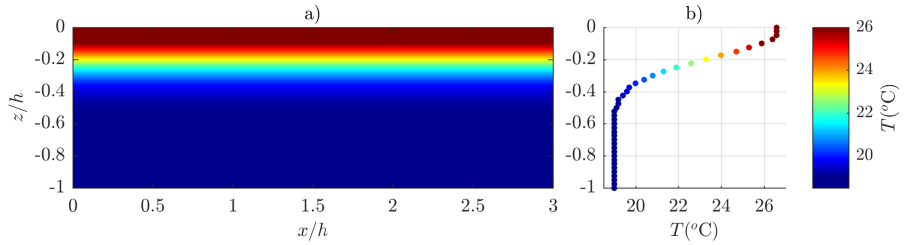

Figure 5. Initial temperature in the fluid domain; a) spatial distribution; b) vertical profile.

Putting aside the problems with averaging of the velocity field and basing on previous comparisons of the higher order solution against experiments in the flume (Paprota, 2020), the general conclusion from the analysis of the results depicted in Figs. 2-4 is that admitting higher-order terms of the Taylor series expansions of the boundary conditions imposed at the moving boundaries leads to more accurate prediction of the time-independent velocity near the wavemaker. This is of significant importance especially for the modeling of wave-induced mixing and the evolution of the water temperature field as the higher-order approach predicts enhanced streaming in layers adjacent to the bottom and the surface. This leads to more intense mixing processes and heat exchange.

3.3 Evolution of temperature field

The modeling of wave-induced vertical mixing in terms of the temperature redistribution in the water column relies on the solution to the two-dimensional boundary-value problem defined by Eqs. (29)-(33). The input parameters being introduced to the governing advection-diffusion equation Eq. (29) are the diffusion coefficient κ_v calculated using the Eqs. (34) and (35) and the time-independent wave velocity field (U, W). The modeling procedure remains in accordance with previously published results ~~Sulisz and Paprota (2019)~~of Sulisz and Paprota (2019) obtained only for weakly-nonlinear velocity field input. The temperature $T_0(z)$ determines the initial thermal state of the fluid (Fig.5).

In Figs. 6-8, the temperature spatial distributions representing the thermal states of undulating water body after 100 s are provided for the test cases listed in Table 1. The results in the plots correspond to the weakly-nonlinear solution and higher-order model predictions of the time-independent wave velocity field. Both methods are compared in order to highlight the effects of nonlinearity on vertical mixing due to waves.

In the direct vicinity of the wavemaker paddle, the initial state of the water temperature is uniformly stratified according to T_0. The moving wavemaker paddle generates regular waves and the layers of water of equal temperature are deformed by the oscillatory motion of the water body according to the time-independent velocity field presented in Figs. 2-4. Advection plays an important role in wave-induced mixing processes as even small changes in the velocity strongly affect the evolution of the temperature field. This implies the major differences between weakly-nonlinear and higher-order predictions of the resultant temperature when the steepness of waves increases. This effect is clearly seen in the Figs. 6-8. As previously stated, the discrepancy between weakly-nonlinear velocities and the velocity predictions admitting higher-order terms in the free-surface

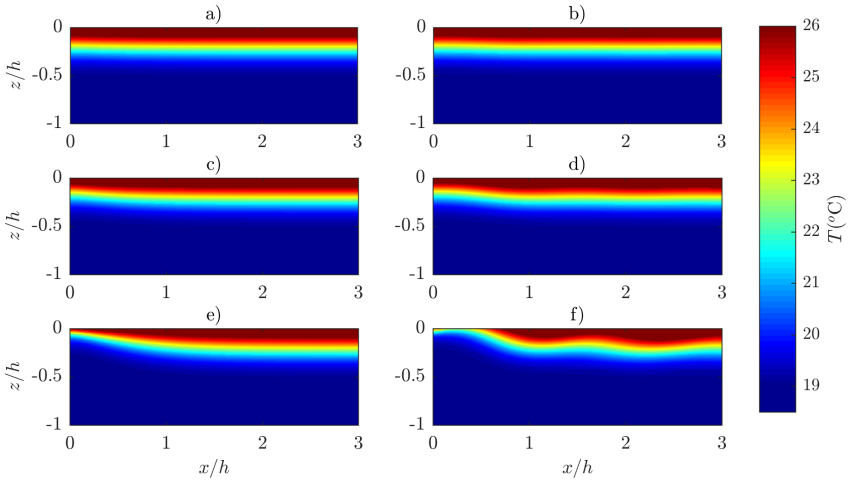

Figure 6. Changes in the temperature field due to waves after 100 s for $kh = 0.5$, a) and b) - $H/h = 0.05$, c) and d) - $H/h = 0.1$, e) and f) - $H/h = 0.2$; weakly-nonlinear theory a), c) and e) (left), higher-order theory b), d) and f) (right).

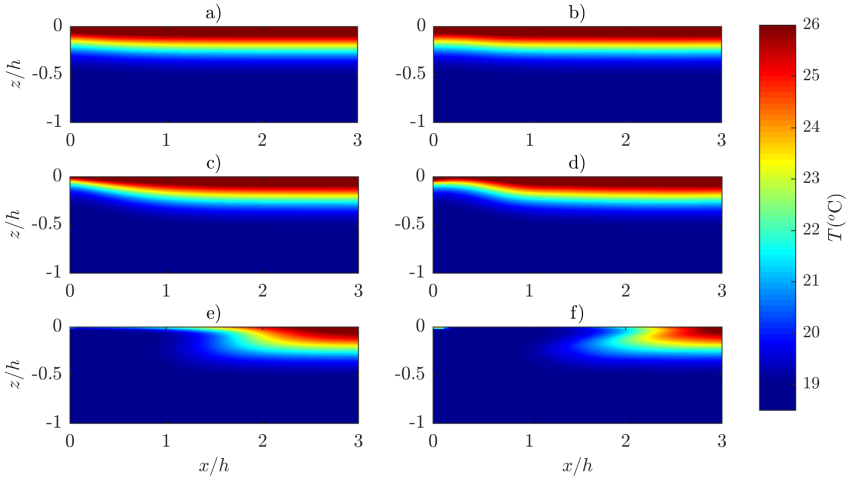

Figure 7. Changes in the temperature field due to waves after 100 s for $kh = 1$, a) and b) - $H/h = 0.05$, c) and d) - $H/h = 0.1$, e) and f) - $H/h = 0.2$; weakly-nonlinear theory a), c) and e) (left), higher-order theory b), d) and f) (right).

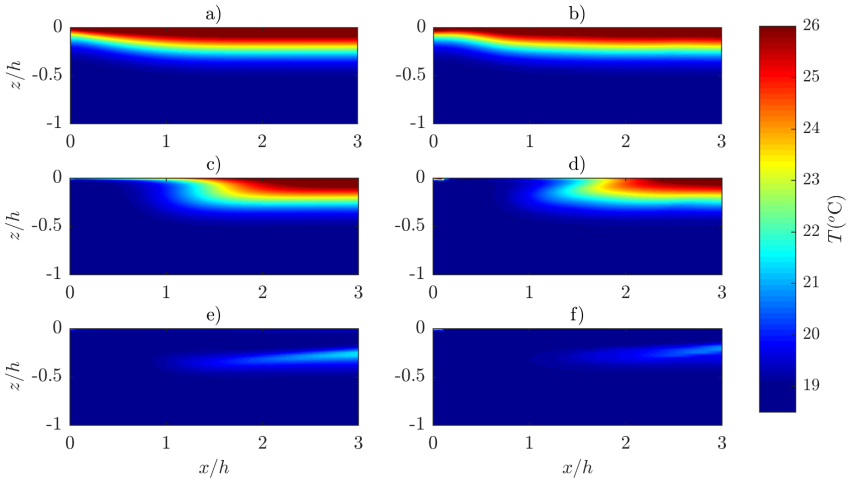

Figure 8. Changes in the temperature field due to waves after 100 s for $kh = 2$, a) and b) - $H/h = 0.05$, c) and d) - $H/h = 0.1$, e) and f) - $H/h = 0.2$; weakly-nonlinear theory a), c) and e) (left), higher-order theory b), d) and f) (right).

boundary conditions grows with increasing steepness and wave nonlinearity (Ursell number) and may even reach 40% in the subsurface layer.

Although the highest relative differences are relevant for the longest waves, the effect of including higher-order terms is most apparent for waves of the largest kh characterized by the highest time-independent velocities. It may be seen in the Fig. 6 that after 100 s the colder water is moved to the surface close to the wavemakeer only for the steepest waves (Fig. 6f) when predicted by higher-order model, while for the corresponding weakly-nonlinear temperature field this process is less intensive (Fig. 6e). Additionally, the higher-order results exhibit some variation of mixing along the flume (Fig. 6f).

In the case of waves characterized by $kh = 1$, the wave-induced mixing is more intensive and for the steepest waves (Fig. 7e and f) the warmer water is moved away from the wavemaker. It should be noticed that higher-order solutions predicts an enhanced streaming near the surface (Fig. 7f). In this way, the decreased water surface temperature affects regions located further away from the wavemaker, when compared to weakly-nonlinear results (Fig. 7). The similar temperature field modification affect the waves of $kh = 2$, but for the lower analyzed height (cf. Figs. 7ef and 8cd). In the case of the highest waves of $kh = 2$ the warmer water is almost completely swept away from the region of direct wavemaker action (Fig. 8e and f).

3.4 Further discussions

Energy input from wind to ocean surface waves is tremendous and exceeds 60 TW (Wang and Huang, 2004). A large amount of energy dissipates and implies stirring and mixing processes in the oceanic mixed layer. A parameterization scheme for surface wave-induced mixing was proposed and numerical experiments indicate that this parameterization affects the performance and outcome of ocean circulation models ~~(Qiao et al., 2004, ?; Xia et al., 2006)~~ (Qiao et al., 2004, 2010; Xia et al., 2006) as well as climate predictions (Song et al., 2007; Huang et al., 2008). Although field observations suggest that surface waves can gen-

erate vertical mixing (Matsuno et al., 2006), it is still difficult to distinguish the mixing ~~originated~~ originating from the variety of processes that accompanied ocean waves. Although the problem of wave-induced vertical mixing is of significant importance for physical oceanographers and climatologists, the research on this subject is still in its infancy. A wave-induced mixing is a very important process from a practical point of view and is a challenging problem for theoretical investigations. The understanding of wave-induced mixing is of fundamental importance for the modeling and accurate prediction of ocean transport processes and climate changes. The problem is that the parameterization scheme applied in the modeling and prediction of ocean surface wave-induced mixing is based on drastic simplifications. Wave models derived using simplifying assumptions cannot be applied to predict ocean surface wave-induced mixing with sufficient accuracy. The present studies clearly show that it is necessary to apply at least a weakly-nonlinear wave theory to obtain reasonable results, while an increased accuracy is possible using advanced nonlinear wave models admitting higher order effects. ~~The present studies provide one~~

One more critical outcome from the point of view of engineers and scientists working on the modeling of ocean transport processes, wave-induced mixing, and climate changes is of signifcant importance. Namely, since it is difficult to distinguish the mixing ~~originated from a variety of processes~~ that accompanied ocean waves, the only chance to provide reliable insight into the wave-induced mixing processes is to conduct laboratory experiments in a wave flume. The repeatable experiments in the well-controlled environment of a wave flume enable us to perform an accurate investigation that is essential in the analysis of the physics of the wave-induced mixing phenomenon. Moreover, a laboratory investigation provides useful data for the analysis of the correlations between spectral and statistical characteristics of wave regimes and wave-induced mixing processes. Finally, laboratory experiments enable us to avoid various side effects and separate the mixing ~~originated from the variety of processes that accompanied~~ from other processes accompanying ocean waves. This is of fundamental importance for understanding of mixing and accurate calibration and verification of numerical models. The problem is that, in addition to progressive laboratory waves, the moving wavemaker represented by the kinematic wavemaker boundary condition, enforces the return current that affects transport processes and wave-induced mixing.

It is the idea behind the present study, which employ numerical wave flume model, to thoroughly analyse wave-induced mixing effects using derived numerical approach and assist further works on experimental fluid mechanics aiming at better understanding of transport processes in the open ocean. To the best of the authors knowledge, the derived wave-induced mixing model is the only available numerical solution that, in addition to nonlinear free-surface boundary conditions, also satisfies the kinematic wavemaker boundary condition. Accordingly, the derived model admits return current and may be applied to quantify and separate the effects of return flow on wave-induced mixing processes. Moreover, the presented results should hopefully improve simple parametric models (Myrhaug et al., 2018). As it was previously mentioned, the derived modelling framework may be modified to cover open ocean conditions and quasi-random sea states using other forms of wave excitation (Paprota, 2019).

4 Conclusions

The applicability of the wave-induced mixing model for waves generated in a wave flume is validated based on the solution admitting higher-order nonlinearities. In the range of wave conditions covering transitional and shallow waters, the weakly-nonlinear results are in reasonable agreement with more accurate pseudo-spectral solution in the case of waves of low to moderate steepness. The general discrepancy grows with increasing the wave height and the wavelength. Contrary to the weakly-nonlinear approach, the higher-order model is able to predict enhanced subsurface streaming affecting the evolution of the surface temperature for more severe sea states. It is due to the fact that the time-independent velocity field predicted by both methods differs especially in the subsurface and near-bottom layer of the oscillating water body.

General ocean circulation models admitting wave-induced vertical mixing but relying on simplified assumptions cannot predict input from mixing with sufficient accuracy. It is necessary to apply at least weakly-nonlinear correction to obtain reasonable approximation. For improved predictions, advanced highly-nonlinear models are preferred, which is confirmed by the present study. Moreover, the derived model allows return current to be correctly quantified in experimental investigations on wave-induced vertical mixing for better interpretation of laboratory results giving more information for further improvements to parametrization schemes.

Data availability. Datasets for this research are available in these in-text data citation reference: Wave-induced mixing in a numerical wave flume submitted with DOI https://doi.org/10.5061/dryad.80gb5mkqw by Maciej Paprota.

Author contributions. The authors contributed equally to this work.

Competing interests. The authors declare no competing interests

References

Babanin, A. V. and Haus, B. K.: On the existence of water turbulence induced by nonbreaking surface waves, J. Phys. Oceanogr., 39, 2675–2679, 2009.

Chen, Y. Y., Hsu, H. C., and Hwung, H. H.: A Lagrangian asymptotic solution for finite-amplitude standing waves, Appl. Math. Comput., 215, 2891–2900, 2009.

Dai, D., Qiao, F., Sulisz, W., Han, L., and Babanin, A. V.: An experiment on the non-breaking surface-wave-induced mixing, J. Phys. Oceanogr., 40, 2180–2188, 2010.

Dean, R. G. and Dalrymple, R. A.: Water wave mechanics for engineers and scientists, vol. 2 of *Advanced Series on Ocean Engineering*, Prentice-Hall, Inc., Englewood Cliffs, 1984.

Dommermuth, D. G. and Yue, D. K. P.: High-order spectral method for the study of nonlinear gravity waves, J. Fluid Mech., 184, 267–288, 1987.

Huang, C., Qiao, F., and Song, Z.: The effect of the wave-induced mixing on the upper ocean temperature in a climate model, Acta Oceanologica Sinica, 27, 104–111, 2008.

Hudspeth, R. T. and Sulisz, W.: Stokes drift in two-dimensional wave flumes, J. Fluid Mech., 230, 209–229, 1991.

Longuet-Higgins, M. S.: Mass transport in water waves, Phil. Trans. R. Soc. A, 245, 535–581, 1953.

Longuet-Higgins, M. S.: Eulerian and Lagrangian aspects of surface waves, J. Fluid Mech., 173, 683–707, 1986.

Matsuno, T., Lee, J.-S., Shimizu, M., Kim, S.-H., and Pang, I.-C.: Measurements of the turbulent energy dissipation rate ε and an evaluation of the dispersion process of the Changjiang Diluted Water in the East China Sea, J. Geophys. Res., 111, C11S09, 2006.

McWilliams, J. C. and Sullivan, P. P.: Vertical mixing by Langmuir circulations, Spill Sci. Techn. Bull., 6, 225–237, 2000.

Myrhaug, D., Wang, H., and Holmedal, L. E.: Stokes transport in layers in the water column based on long-term wind statistics, Oceanologia, 61, 522–526, 2018.

Paprota, M.: On pressure forcing techniques for numerical modelling of unidirectional nonlinear water waves, Appl. Ocean Res., 90, 101 857, 2019.

Paprota, M.: Experimental study on spatial variation of mass transport induced by surface waves generated in a finite-depth laboratory flume, J. Phys. Oceanogr., 50, 3501–3511, 2020.

Paprota, M. and Sulisz, W.: Particle trajectories and mass transport under mechanically generated nonlinear water waves, Phys. Fluids, 30, 102 101, 2018.

Paprota, M. and Sulisz, W.: Improving performance of a semi-analytical model for nonlinear water waves, J. Hydro-environ. Res., 22, 38–49, 2019.

Paprota, M., Sulisz, W., and Reda, A.: Experimental study of wave-induced mass transport, J. Hydraul. Res., 54, 423–434, 2016.

Press, W. H., Flannery, B., Teukolsky, S. A., and Vetterling, W. T.: Numerical Recipes, Cambridge University Press, Cambridge, UK, 1988.

Qiao, F., Yuan, Y., Yang, Y., Zheng, Q., Xia, C., and J.Ma: Wave-induced mixing in the upper ocean: distribution and application to a global ocean circulation model, Geophys. Res. Lett., 31, L11 303, 2004.

Qiao, F., Yuan, Y., Ezer, T., Xia, C., Yang, Y., Lu, X., and Song, Z.: A three-dimensional surface wave-ocean circulation coupled model and its initial testing, Ocean Dyn., 60, 1339–1355, 2010.

Qiao, F., Song, Z., Bao, Y., Song, Y., Shu, Q., Huang, C., and Zhao, W.: Development and valuation of an Earth System Model with surface gravity waves, J. Geophys. Res., 118, 4514–4524, 2013.

Shu, Q., Qiao, F., Song, Z., Xia, C., and Yang, Y.: Improvement of MOM4 by including surface wave-induced vertical mixing, Ocean Model., 40, 42–51, 2011.

Song, Z., Qiao, F., Yang, Y., and Yuan, Y.: An improvement of the too cold tongue in the tropical Pacific with the development of an ocean-wave-atmosphere coupled numerical model, Prog. Nat. Sci., 17, 576–583, 2007.

Sulisz, W. and Hudspeth, R. T.: Complete second-order solution for water waves generated in wave flumes, J. Fluids Struct., 7, 253–268, 1993.

Sulisz, W. and Paprota, M.: Theoretical and experimental investigations of wave-induced vertical mixing, Math. Probl. Eng., 2015, 2015.

Sulisz, W. and Paprota, M.: On modeling of wave-induced vertical mixing, Ocean Eng., 194, 106 622, 2019.

Wang, W. and Huang, R. X.: Wind energy input to the surface waves, J. Phys. Oceanogr., 34, 1276–1280, 2004.

West, B. J., Brueckner, K. A., and Janda, R.: A new numerical method for surface hydrodynamics, J. Geophys. Res., 92, 11 803–11 824, 1987.

Xia, C., Qiao, F., Yang, Y., Ma, J., and Yuan, Y.: Three-dimensional structure of the summertime circulation in the Yellow Sea from a wave-tide-circulation coupled model, J. Geophys. Res., 111, C11S03, 2006.